Ships and Offshore Structures

ISSN: (Print) (Online) Journal homepage: https://www.tandfonline.com/loi/tsos20

Numerical study of distributed hydrodynamic forces on a circular heave plate by large-eddy simulations with volume of fluid method

Shining Zhang & Takeshi Ishihara

To cite this article: Shining Zhang & Takeshi Ishihara (2020) Numerical study of distributed hydrodynamic forces on a circular heave plate by large-eddy simulations with volume of fluid method, Ships and Offshore Structures, 15:6, 574-586, DOI: 10.1080/17445302.2019.1661630

To link to this article: https://doi.org/10.1080/17445302.2019.1661630

Published online: 09 Sep 2019.

SHIPS AND OFFSHORE STRUCTURES
2020, VOL. 15, NO. 6, 574–586
https://doi.org/10.1080/17445302.2019.1661630

Taylor & Francis
Taylor & Francis Group

Numerical study of distributed hydrodynamic forces on a circular heave plate by large-eddy simulations with volume of fluid method

Shining Zhang[a] and Takeshi Ishihara[b]

[a]Climate Change & Environment Research Division, Economy & Technology Research Institute, Global Energy Interconnection Development and Cooperation Organization, Beijing, People's Republic of China; [b]Department of Civil Engineering, School of Engineering, The University of Tokyo Hongo, Tokyo, Japan

ABSTRACT

Distributed hydrodynamic forces on circular heave plates are investigated by large-eddy simulation (LES) with volume of fluid (VOF) method. First, the predicted added mass and drag coefficients for a whole heave plate is validated by published experimental data. The distributions of hydrodynamic loads on the circular heave plates are then investigated. It is found that maximum dynamic pressure occurs at the plate centre and decreases monotonically towards the outer regions. Finally, formulas of distributed added mass and drag coefficients in the radial direction are proposed based on present numerical simulations, and effects of aspect ratio and diameter ratio on the distributed added mass and drag coefficients are investigated.

ARTICLE HISTORY
Received 5 January 2019
Accepted 10 June 2019

KEYWORDS
Distributed hydrodynamic load; large-eddy simulation; formulas of the distributed added mass and drag coefficients

Nomenclature

r_t	aspect ratio of heave plate thickness to diameter
R_d	diameter ratio of heave plate diameter to column diameter
C_a	added mass coefficient
C_p	dynamic pressure around heave plate
C_d	drag coefficient
$F_H(t)$	time-varying hydrodynamic force
D_c	column diameter
F_b	buoyance force
D_{Hp}	heave plate diameter
$F_K(t)$	time-varying hydrostatic force
t_{Hp}	heave plate thickness
r	normalised radial distance
	the characteristic area of the heave plate
h_p	model draft

1. Introduction

Floating offshore wind turbines (FOWTs) are a promising innovation used to capture huge potential offshore wind energy in deep water areas. The world's first full-scale 2.3 MW spar-type FOWT in Hywind project was installed in Norway by Statoil Hydro in 2009 (Hywind 2009), and the second prototype was the 2 MW semi-submersible FOWT in WindFloat project deployed in Portugal by Principle Power in 2011 (WindFloat 2011). In Japan, a 2 MW spar-type FOWT in GOTO-FOWT project was built off the coast of Kabashima in 2013 (Utsunomiya et al. 2014). In addition, another 2 MW semi-submersible FOWT and a 7 MW V-shape semi-submersible FOWT in Fukushima FORWARD project were completed off the coast of Fukushima in 2013 and 2015, respectively (Fukushima 2013). In the semi-submersible and advanced spar FOWTs, heave plates are usually adopted to reduce heave motions and to shift heave resonance periods out of the first-order wave energy range (Lopez-Pavon and Souto-Iglesias 2015). Some new concepts of floating platform have been adopted. A substation and a new 5 MW FOWT constructed in Fukushima FORWARD project (Fukushima 2013) adopt an advanced spar consisting of multiple heave plates. The hydrodynamic characteristics of the heave plates are key factors during designs of platform that support the FOWT.

Hydroelastic vibration and plate mode shapes of circular plates have been investigated in the studies by Amabili et al. (1996) and Askari et al. (2013). Morison's equation and potential theory are widely used to predict hydrodynamic loads on the heave plates of FOWTs (Jonkman 2007; Phuc and Ishihara 2007; Kvittem et al. 2012; Waris and Ishihara 2012; Browning et al. 2014; Ishihara and Zhang 2019). The hydrodynamic coefficients, namely, added mass coefficient and drag coefficient (hereinafter referred to as C_a and C_d, respectively) of the heave plates need to be determined when evaluating hydrodynamic loads on heave plates by either Morison's equation or potential theory. The hydrodynamic coefficients of the heave plates as a whole have been intensively studied by means of water tank tests (Li et al. 2013; Lopez-Pavon and Souto-Iglesias 2015; Zhang and Ishihara 2018), numerical simulations (Tao and Thiagarajan 2003a; Tao and Thiagarajan 2003b; Tao et al. 2004; Tao and Cai 2004; Tao et al. 2007; Yang et al. 2014; Garrido-Mendoza et al. 2015; Lopez-Pavon and Souto-Iglesias 2015; Zhang and Ishihara 2018), or empirical formulas (Tao and Cai 2004; Tao et al. 2007; Zhang and Ishihara 2018). However, the time series of distributed load which is absolutely necessary for structural design is seldomly studied. The distributed load could be expressed by a sum of inertia force and damping force as in Morison's equation. Or, damping force expressed by drag coefficient is combined into potential theory

CONTACT Shining Zhang shining-zhang@geidco.org Climate Change & Environment Research Division, Economy & Technology Research Institute, Global Energy Interconnection Development and Cooperation Organization, 100031 Beijing, People's Republic of China

when evaluating the hydrodynamic loads. Thus, no matter which theory is used, distributed hydrodynamic coefficients are needed to be provided for structural design.

Water tank test is one of the ways to determine the hydrodynamic load distribution by measuring dynamic pressure distribution on the plate (Lopez-Pavon and Souto-Iglesias 2015). In the study by Lopez-Pavon and Souto-Iglesias (2015), the dynamic pressure distribution on the upper and lower surface of a circular heave plate was measured. It was observed that dynamic pressure on lower surface was larger than that on its corresponding upper surface. In addition, dynamic pressure near the plate centre was larger than that on the outer regions. This indicates that the hydrodynamic load distribution on the plate is not uniform.

Computational fluid dynamics (CFD) is an alternative way to investigate the hydrodynamic load distribution on offshore structures (Chandrasekaran and Madhavi 2014; Chandrasekaran et al. 2015; Chandrasekaran and Madhavi 2015a; Chandrasekaran and Madhavi 2015b; Chandrasekaran and Madhavi 2015c; Chandrasekaran and Madhavi 2016). Holmes et al. (2001) studied the hydrodynamic coefficients of a square heave plate via a finite element method with LES turbulent model. Detailed load distribution on the plate was obtained, but the distributed C_a and C_d was not evaluated. As concluded from previous studies (Tao and Thiagarajan 2003a; Tao and Thiagarajan 2003b; Tao and Cai 2004; Lopez-Pavon and Souto-Iglesias 2015), the C_a and C_d are functions of aspect ratio, diameter ratio and KC number. However, the effect of these parameters on distributed C_a and C_d has not been studied yet.

Empirical formulas are cost-effective compared with water tank tests and numerical simulations, making them beneficial for optimised design of heave plates. The C_a and C_d for a whole heave plate are studied in the references (Graham 1980; Tao and Cai 2004; Tao et al. 2007; Philip et al. 2013; Zhang and Ishihara 2018). However, formulas of the distributed C_a and C_d have not been proposed yet.

In this study, the effects of geometrical parameters and KC number on the radially distributed C_a and C_d of circular heave plates are systematically investigated. Section 2 describes governing equations with LES model and VOF method, grid arrangement, numerical schemes and boundary conditions. In Section 3, the validation of numerical results by published experimental data is performed and the mechanism of hydrodynamic load distribution with the flow pattern is clarified. In addition, the distributed C_a and C_d are defined and investigated considering the effect of geometrical parameters, i.e. diameter ratio and aspect ratio. Finally, formulas of radially distributed C_a and C_d are proposed. The conclusions are summarised in Section 4.

2. Numerical model

The governing equations and LES turbulent model with VOF are given in Section 2.1. The computational domain is described in Section 2.2. Section 2.3 presents numerical schemes and boundary conditions. The hydrodynamic coefficients are defined in Section 2.4.

2.1. Governing equation

Considering Reynolds-averaged Navier–Stokes (RANS) turbulence models (SST) overestimated drag coefficient as observed in Figure 1, large-eddy simulation (LES) is adopted in this study to simulate the flows around the plate. The Boussinesq hypothesis is employed, and the standard Smagorinsky–Lilly model is used to calculate the subgrid-scale (SGS) stresses. The governing equations in Cartesian coordinates are expressed in the form of tensor as

$$\frac{\partial \widetilde{u}_i}{\partial x_i} = 0 \tag{1}$$

$$\frac{\partial \rho \widetilde{u}_i}{\partial t} + \frac{\partial \rho \widetilde{u}_i \widetilde{u}_j}{\partial x_j} = -\frac{\partial \widetilde{p}}{\partial x_i} + \frac{\partial}{\partial x_j}\left[\mu\left(\frac{\partial \widetilde{u}_i}{\partial x_j} + \frac{\partial \widetilde{u}_j}{\partial x_i}\right)\right] - \frac{\partial \tau_{ij}}{\partial x_j} + \rho g_i \tag{2}$$

where $\widetilde{u}_i$ and $\widetilde{p}$ are filtered mean velocity and pressure, respectively. μ is dynamic viscosity, ρ is the density of fluid, g_i is the component of the gravitational acceleration g in the direction of the coordinate x_i. $\tau_{ij} = \rho(\widetilde{u_i u_j} - \widetilde{u}_i \widetilde{u}_j)$ is SGS (subgrid-scale) stress resulting from the filtering operations, and it is modelled as

$$\tau_{ij} = -2\mu_t \widetilde{S}_{ij} + \frac{1}{3}\tau_{ii}\delta_{ij} \tag{3}$$

where μ_t is subgrid-scale turbulent viscosity and $\widetilde{S}_{ij}$ is the rate-of-strain tensor for the resolved scale defined as

$$\widetilde{S}_{ij} = \frac{1}{2}\left(\frac{\partial \widetilde{u}_i}{\partial x_j} + \frac{\partial \widetilde{u}_j}{\partial x_i}\right) \tag{4}$$

Smagorinsky model is used for the subgrid-scale turbulent viscosity, μ_t and is defined as

$$\mu_t = \rho L_S^2 |\widetilde{S}| = \rho L_S^2 \sqrt{2\widetilde{S}_{ij}\widetilde{S}_{ij}} \tag{5}$$

Here, L_S is the mixing length for subgrid-scales, and it is given by

$$L_S = \min(\kappa\delta, C_s V^{1/3}) \tag{6}$$

where κ is the von Karman constant, 0.42, C_s is Smagorinsky constant. $C_s = 0.032$ is used in the present study following suggestion in reference (Oka and Ishihara 2009) since the second-order implicit discretisation scheme is utilised in this study, in which numerical diffusions are small and positive. δ is the distance to the closest wall and is the volume of a computational cell.

Volume of fluid (VOF) model is used in this study to model air and water. The volume fraction of water will be solved to capture the interface between air and water. Continuity equation for the volume fraction of water, α_w, reads

$$\frac{1}{\rho_w}\left[\frac{\partial}{\partial t}(\alpha_w \rho_w) + \nabla(\alpha_w \rho_w \vec{v}_w)\right] = 0 \tag{7}$$

where ρ_w is the water density.

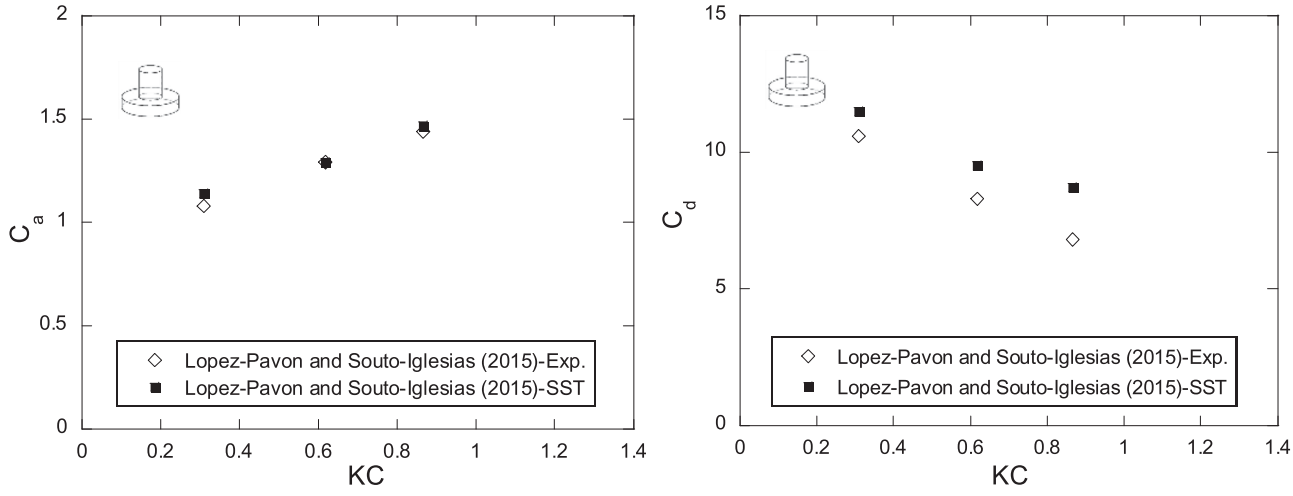

Figure 1. Comparison of predicted added mass and drag coefficients by SST model and measured those for a single heave plates with different KC number in reference (Lopez-Pavon and Souto-Iglesias 2015) under condition of $\omega/\omega_r = 1.6$.

2.2. Configuration of a circular heave plate and computational domain

Schematic of the heave plate model is shown in Figure 2. A circular column is attached on the upper surface of the circular heave plate. The dimensions of the model are listed in Table 1. Draft of the heave plate is 500, and 85 mm of the model is above the still water level (SWL). Diameter of the heave plate is 334 mm. The thickness of the heave plate varies from 1.67 mm to 133.6 mm, which corresponds to the aspect ratio,$r_t(= t_{Hp}/D_{Hp})$, in the range from 0.005 to 0.4. The diameter of the column varies from 50 mm to 133.6 mm, which corresponds to the diameter ratio, $R_d = D_{Hp}/D_c$, ranging from 2.5 to 6.68. In order to investigate distributed hydrodynamic force on the plate in its radial direction, the heave plate is divided into nine annular panels as shown in Figure 2(b). The diameter of P1 is 66.8 mm, and radial spacing between each adjacent plane is 16.7 mm.

Quality of computational grid plays a crucial role in the reliability of numerical results. For this reason, a simple grid-convergence is studied to choose a reasonable grid system following the study by Zhang and Ishihara (2018). The whole computational domain and final grid is displayed in Figure 3 (a). The computational domain is divided into two subdomains

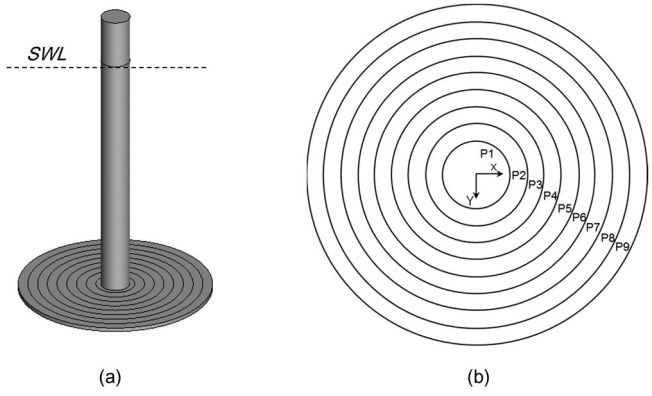

Figure 2. Schematic of the heave plate and divided panels (a) Schematic of a heave plate and (b) Divided panels at bottom of the heave plate.

Table 1. Model geometry.

Item	Notation	Dimension (mm)
Model draft	h_p	436.7–568.6
Column diameter	D_c	50–133.6
Heave plate diameter	D_{Hp}	334
Heave plate thickness	t_{Hp}	1.67–133.6

with respect to two phases. The lower subdomain is used to simulate the phase of water, and its depth is 3.1 h_p from still water level (SWL). The upper subdomain that considers the phase of air has a height of 0.6 h_p above the SWL. In order to mitigate the reflecting flow from the boundary, side walls are located sufficiently far away from the model. The distance between the model and inlet and outlet is 40 D_c and 52 D_c, respectively (D_c is the diameter of centre column). Structured grid is generated in the computation domain, and the grid is refined at the locations where substantial flow separation is expected as shown in Figure 3(b). As an attempt to capture the shape of free surface, the grid is refined near SWL as well. As listed in Table 1, several configurations of heave plates are simulated in this study. The total grid number in the computational domain, therefore, differs in each model. The grid number ranges from 3.5 million to 3.9 million in those models. Time step dependence has been studied in the study by Zhang and Ishihara (2018), and 0.001s is finally used in this study to take into account the numerical accuracy and computational efficiency. Grid parameters near the column and heave plate are listed in Table 2.

2.3. Numerical scheme and boundary conditions

A finite volume method is employed for the present time-dependent numerical simulations. A second-order central difference scheme is used for the convective and viscous terms. A first-order implicit scheme is employed for the unsteady term in momentum equation (see Equation (2)), while explicit approach is adopted for time discretisation in volume fraction equation as shown in Equation (7). Courant number is 0.25. The pressure-based segregated algorithm is

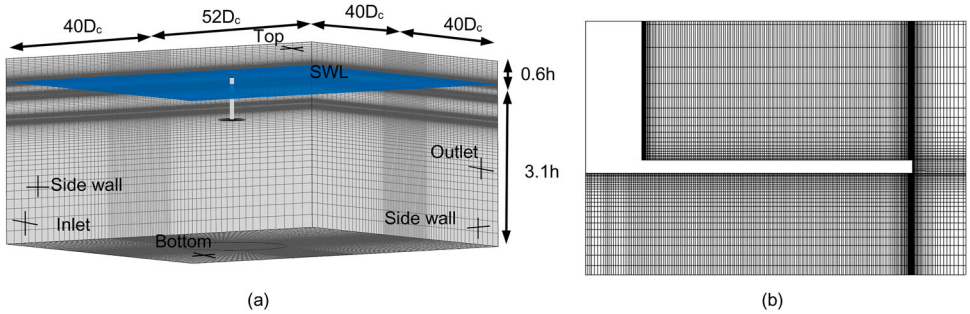

Figure 3. Computational domain and grids around the model. The distance between the model and inlet and outlet boundary is 40 D_c and 52 D_c, respectively (D_c is the diameter of the centre column). Structured grid is generated in the computation domain, and the grid is refined at the locations where substantial flow separation is expected (a) Computational domain and (b) Grids around the column and heave plate. (This figure is available in colour online.)

Table 2. Grid parameters near the column and heave plate.

Item	Value and dimension
First layer in the radial direction	0.257 mm
First layer in the vertical direction	0.6 mm
Expanding factor	1.0–1.2
Grid number	3.5–3.9 million

used to solve the non-linear and coupled governing equation. The pressure-implicit with splitting of operators (PISO) algorithm is chosen to decrease the iterations for the pressure–velocity coupling solution. 20 iterations with PISO pressure-velocity coupling algorithm are used to ensure the divergence-free velocity field. Table 3 summaries the numerical scheme used in this study. The governing equations are solved by a software ANSYS Fluent. The time step convergence and grid dependency are checked as mentioned by Oka and Ishihara (2009) and Stern et al. (2001).

Forced oscillation tests are carried out in the numerical simulations to evaluate the hydrodynamic coefficients, and dynamic mesh with layering mesh update method is utilised to simulate the movement of the model. The top of air phase and the bottom of water phase are treated as stationary boundaries, while the model is oscillated up and down. Both split factor (a_s) and collapse factor (a_c) for the cells near the boundaries are 0.4 with respect to the first cell height (h_1) at moving boundaries. The layer of cells adjacent to the moving boundary is split or merged with layer of cells next to it based on the height of cells. The cell heights are allowed to increase until $h > (1 + a_s)h_1$, and the cell heights can be compressed until $h > a_c h_1$. The governing equations are solved based on newly determined cell coordinate.

Table 3. Numerical scheme.

Item	Scheme
Turbulence model	Smagorinsky-Lilly (Smagorinsky 1963) ($C_s = 0.032$)
Spatial discretisation method	Second-order central difference scheme
Time discretisation method for the momentum equation	First-order implicit scheme
Time discretisation method for volume fraction equation	Explicit scheme
Pressure–velocity coupling	Pressure-implicit with splitting of operators (PISO)
Courant number	0.25
Dynamic mesh	Layering

Boundary conditions are summarised in Table 4. No-slip wall condition is adopted for the surface of the model. Symmetry conditions are utilised for both the top of air phase, the bottom of water phase and the side wells, which indicates the shear stress at the boundary is zero. Outflow boundary condition (zero gradient of velocity) is applied to the inlet and outlet as in the water tank test. In the LES model, the wall shear stress is obtained from the laminar stress–strain relationship when the centroid of wall adjacent cell is in the laminar sublayer with the height of $y+ = 11.25$ as shown in Fluent Theory Guide (Ansys 2012). If the mesh is too coarse to resolve the laminar sublayer, it is assumed that the centroid of the wall adjacent cell falls within the logarithmic region of the boundary layer, and the law-of-the-wall is employed. The grid and time-step independencies have been systematically carried out for a multi-plates model studied by Zhang and Ishihara (2018) and the same parameters are used in this study.

2.4. Definition of hydrodynamic coefficients

In the numerical simulation, the model is vertically oscillated in a sinusoidal form, i.e.

$$z(t) = a \ \sin(\omega t) \tag{8}$$

where $z(t)$ is the displacement in the vertical direction from the still water level (SWL), a is the oscillating amplitude, ω is the oscillating frequency ($= 2\pi/T$) and T is the oscillating period.

The oscillating parameters used in present numerical simulation are given in Table 5. KC number and the frequency number β shown in the table are defined as follows:

$$KC = \frac{2\pi a}{D_{Hp}} \tag{9}$$

$$\beta = \frac{R_e}{KC} = \frac{D_{Hp}^2}{T\nu} \tag{10}$$

Table 4. Boundary conditions.

Item	Boundary conditions
Model walls	No-slip wall
Top of air phase	Symmetry
Bottom of the water phase	Symmetry
Side walls	Symmetry
Inlet and outlet	Outflow (zero gradient of velocity)

Table 5. Oscillation parameters in numerical simulations.

Parameter	Notation	Value
Oscillating amplitude (m)	a	0.02
Oscillating period (s)	T	0.8
KC number	KC	0.38
Frequency parameter	β	139,028

where R_e is the Reynolds number D_{Hp} is the circumcircle diameter of heave plate Hp and ν is the kinematic viscosity of water.

The time series of the predicted hydrodynamic force, $F_H(t)$, acting on the whole heave plate is obtained by subtracting the buoyancy force, F_b, and hydrostatic force, $F_K(t)$, from the total predicted force, $F(t)$ i.e.

$$F_H(t) = F(t) - F_b - F_K(t) \tag{11}$$

F_b, and $F_K(t)$ are given by

$$F_b = \rho_w g \forall \tag{12}$$

$$F_K(t) = -K_R\, z(t) \tag{13}$$

where ρ_w is water density, g is the gravitational acceleration, $\forall$ is the displaced volume by the model at its mean position, K_R is the hydrostatic stiffness with $K_R = \rho_w g A_w$ and A_w is the water plane area.

The hydrodynamic force defined in Equation (11) is expressed in the form of Morison's equation as follows:

$$\begin{aligned} F_H(t) &= -C_a M_{at}\, \ddot{z}(t) - 0.5 C_d \rho_w A |\dot{z}(t)| \dot{z}(t) \\ &= \frac{1}{3} C_a \rho_w D_{Hp}^3 a\omega^2 \sin(\omega t) - \frac{1}{2} C_d \rho_w A (a\omega)^2 |\cos(\omega t)| (\cos(\omega t)) \end{aligned} \tag{14}$$

where C_a is added mass coefficient, C_d is drag coefficient, $M_{at} = (1/3\rho_w D_{Hp}^3)$ is the theoretical added mass of the heave plate as defined in reference (Sarpkaya 2010), and $A = (1/4\pi D_{Hp}^2)$ is the characteristic area of the heave plate and $\dot{z}(t)$ and $\ddot{z}(t)$ are the velocity and acceleration of the model motion, respectively.

As introduced in reference (Sarpkaya 2010), Fourier averages of C_a and C_d are obtained as follows:

$$\begin{aligned} C_a &= \frac{\int_0^T F_H(t) \sin(\omega t) dt}{\frac{1}{3}\rho_w D_{Hp}^3 a\omega^2 \int_0^T \sin^2(\omega t) dt} \\ &= \frac{3}{\pi \omega a \rho_w D_{Hp}^3} \int_0^T F_H(t) \sin(\omega t) dt \end{aligned} \tag{15}$$

$$\begin{aligned} C_d &= -\frac{\int_0^T F_H(t) \cos(\omega t) dt}{\frac{1}{2}\rho_w A (\omega a)^2 \int_0^T |\cos(\omega t)| (\cos(\omega t)) \cos^2(\omega t) dt} \\ &= -\frac{3}{4\rho_w A \omega a^2} \int_0^T F_H(t) \cos(\omega t) dt \end{aligned} \tag{16}$$

Parameters used for the calculation of C_a and C_d are listed in Table 6.

Table 6. Parameters used for the calculation of C_a and C_d.

Item	Notation	Value
Characteristic area (m^2)	A	0.0876
Displaced volume (m^3)	$\forall$	0.001~0.0178
Water density (kg/m^3)	ρ_w	1000
Hydrostatic stiffness (N/m)	$K_R = \rho_w g A_w = \rho_w g \pi D_c^2/4$	19.26~137.53

3. Numerical results and formulas of hydrodynamic coefficients

In Section 3.1, the numerical results are validated by comparing the identified hydrodynamic coefficients with those obtained from published experimental data. The distributed hydrodynamic coefficients are then presented along with the discussion about the effect of aspect ratio as well as diameter ratio in Section 3.2. Formulas of radially distributed hydrodynamic coefficients are proposed in Section 3.3.

3.1. Integral hydrodynamic coefficients

The time series of the predicted hydrodynamic force is presented in a non-dimensional form as follows:

$$C_F(t^*) = \frac{F_H(t)}{\frac{1}{2}\rho_w A (\omega a)^2};\ t^* = \frac{t}{T} \tag{17}$$

where $F_H(t)$ is the predicted hydrodynamic force according to Equation (11), $A = \pi D_{Hp}^2/4$ is the characteristic area of the heave plate and t^* is the non-dimensional time.

Time series of predicted hydrodynamic force becomes stable after the initial first period. In order to prevent the effect of initial solution on accuracy of evaluated hydrodynamic coefficients, the simulated data over period 3~5 are chosen as the data sample. The time series of non-dimensional hydrodynamic force for one typical case is illustrated in Figure 4. The predicted hydrodynamic force associated with C_a and C_d in the Morison's equation is also plotted in the figure. The

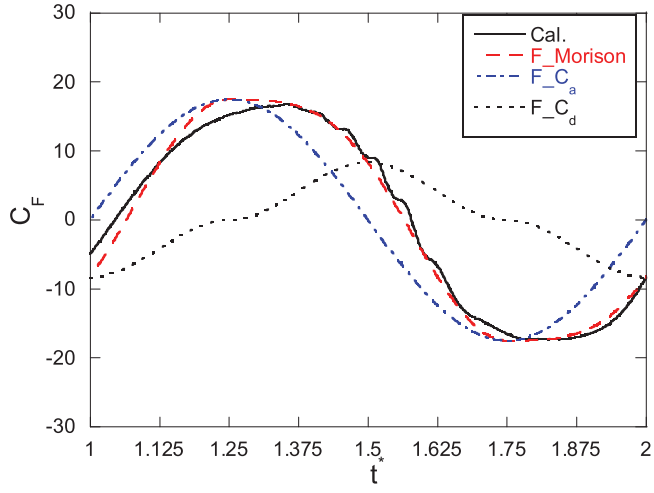

Figure 4. Time series of non-dimensional hydrodynamic force acting on the whole heave plate (KC = 0.38, r_t = 0.2, R_d = 6.68). Cal. is the predicted hydrodynamic force from the present numerical simulation, F_Morison represents reproduced hydrodynamic force by Morison's equation with identified added mass and drag coefficient, F_Ca means the added inertia force component and F_Cd is the drag force component in Morison's equation. (This figure is available in colour online.)

hydrodynamic force predicted by Morison's equation matches well with the numerical results in terms of both amplitude and phase. In addition, the amplitude of non-dimensional force in this study is about 18 and resulting C_a agrees well with that measured by Lopez-Pavon and Souto-Iglesias (2015). C_d exhibits some differences, since the frequency parameter, β, differs between these two cases. Inertia force as shown in Figure 4 is larger than the drag force since the KC number of 0.38 in the present simulation is relatively small.

Figure 5 shows the variation of the predicted C_a and C_d and those by the previous studies with diameter ratios. In the experiment by Tao and Dray (2008), diameter of the heave plate is 400 mm, thickness is 8 mm and the diameter of column is measured as 48.8 mm from their experimental figure. In the experiment by Lopez-Pavon and Souto-Iglesias (2015), diameter of the heave plate is 1000 mm, thickness is 5 mm and the diameter of column is 350 mm. As shown in Figure 5(a), C_a slightly increases as the plate diameter ratio increases. This is because the wet surface at upper surface of heave plate is larger when the diameter of attached column decreases. The predicted C_a shows good agreement with the measurement. By contrast, C_d shown in Figure 5(b) does not increase monotonically with the increase in the diameter ratio because the viscous damping is mainly contributed by the vortex shedding at the outer edges of the heave plate. Increasing the wet surface at upper surface of heave plate has a negligible effect on the vortex shedding outside of the centre region. In the interactive vortex shedding regime, interaction of positive and negative vortex formed at the upper surface and lower surface of heave plate will diffuse the vortex and decrease the drag force compared with that in the uni-directional vortex shedding regime as mentioned by Tao and Thiagarajan (2003a).

Figure 6 illustrates variation of the predicted C_a and C_d with aspect ratios. It can be found from Figure 6(a) that C_a is independent of the aspect ratio. This is because the change in thickness has no influence on the characteristic area of upper and lower surfaces of the heave plate, and thus has no remarkable impact on dynamic pressure distribution in phase with acceleration. In contrast, C_d is strongly dependent on the aspect ratio as shown in Figure 6(b). It is found that C_d decreases as the aspect ratio increases. Variations of the thickness generate distinct vortex shedding patterns, which have been reported in the references (Tao and Thiagarajan 2003a; Tao and Thiagarajan 2003b; Zhang and Ishihara 2018). Figure 7 reveals the instantaneous vortex shedding around the heave plate with two representative aspect ratios at time $t = 0$ when the heave plate is moving upward from its mean position. The uni-directional vortex shedding happens in the case of small aspect ratio as shown in Figure 7(a), while the interactive vortex shedding is observed for the case of large aspect ratio in Figure 7(b). It is the emerging interaction of vortex shedding from upper and lower surfaces of the heave plate that leads to the decreased C_d. As the aspect ratio further increases, independent vortex shedding pattern appears as reported by Tao and Thiagarajan (2003b).

3.2. Distributed hydrodynamic coefficients

The predicted hydrodynamic force acting on each panel as shown in Figure 2 includes the force caused by hydrostatic pressure, which is excluded when evaluating the hydrodynamic coefficients. The hydrodynamic force acting on the upper and lower surfaces, $F^U_{H,Pi}(t)$ and $F^L_{H,Pi}(t)$ of each panel is obtained as follows:

$$F^U_{H,Pi}(t) = F^U_{Pi}(t) + \rho_w g h^U_{Pi} A^U_{Pi} - \rho_w g A^U_{Pi} z(t) \tag{18}$$

$$F^L_{H,Pi}(t) = F^L_{Pi}(t) - \rho_w g h^L_{Pi} A^L_{Pi} + \rho_w g A^L_{Pi} z(t) \tag{19}$$

where h^U_{Pi} and h^L_{Pi} are the depths of the upper and lower surfaces of panel Pi, A^U_{Pi} and A^L_{Pi} are the characteristic areas of the upper and lower surface of panel Pi, respectively.

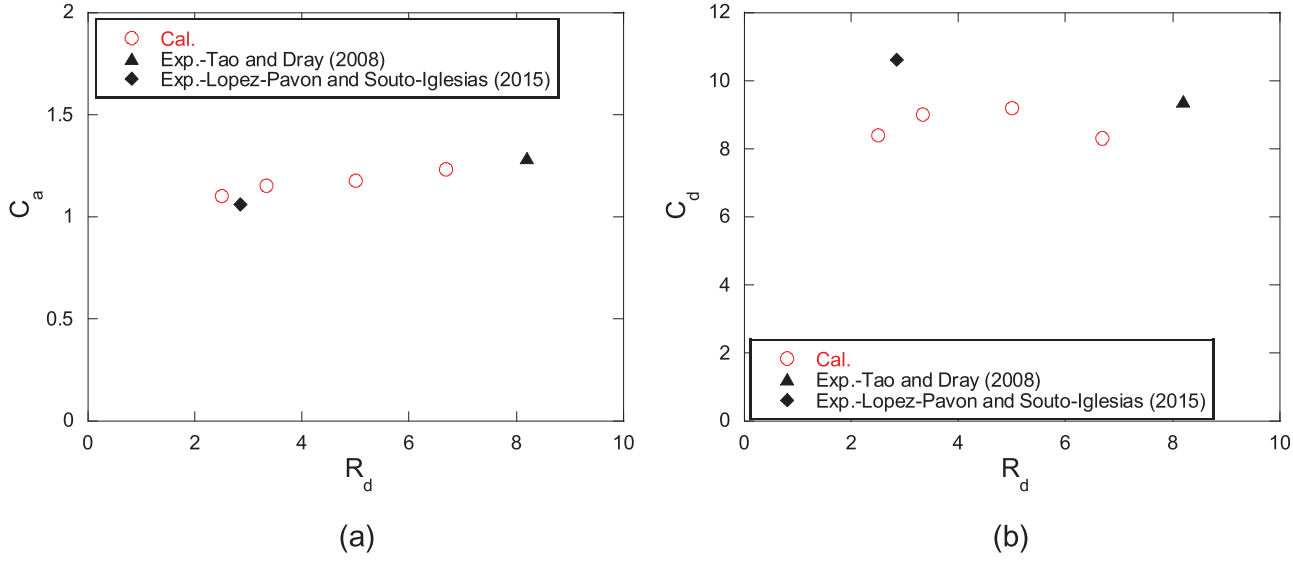

Figure 5. Variation of the added mass and drag coefficients with the diameter ratios. In the experiment by Tao, L and Dray, D (KC = 0.4, $r_t = 0.2$), averaged C_a and C_d in three oscillating frequencies (f = 0.1,0.5,1 Hz) are plotted in the above figure. In the experiment by Lopez-Pavon, C. and Souto-Iglesias (KC = 0.308, $r_t = 0.005$), averaged C_a and C_d in all oscillating frequencies are plotted in this figure (a) Added mass coefficient and (b) Drag coefficient. (This figure is available in colour online.)

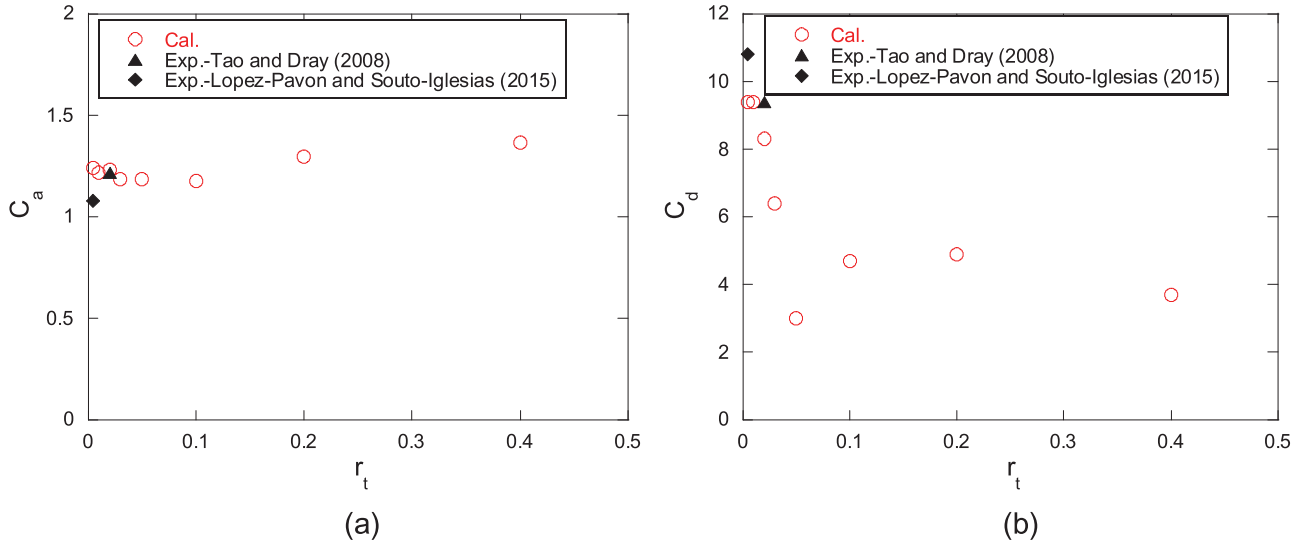

Figure 6. Variation of the added mass and drag coefficients with the aspect ratios. In the experiment by Tao, L and Dray, D (KC = 0.4, R_d = 8.2), averaged C_a and C_d in three oscillating frequencies (f = 0.1,0.5,1 Hz) are plotted in this figure. In the experiment by Lopez-Pavon, C. and Souto-Iglesias (KC = 0.308, R_d = 2.86), averaged C_a and C_d in all oscillating frequencies are shown in this figure (a) Added mass coefficient and (b) Drag coefficient. (This figure is available in colour online.)

The dynamic pressure is defined as

$$C_p = \frac{p - \rho_w g h_c}{1/2\rho_w(\omega a)^2} \tag{20}$$

where p is the pressure, which contains hydrodynamic pressure and hydrostatic pressure, h_c is the depth of the computational cell from the still water level.

Figure 8 exhibits the time series of non-dimensional hydrodynamic force on the upper and lower surfaces of several panels for the case of r_t = 0.02 and R_d = 6.68. Here, the characteristic area of each corresponding panel is used in the non-dimensional form as in Equation (17). From Figure 8(a), the maximum hydrodynamic force on the upper surface of panels P1∼P7 occurs at time t = 2/8 T when the acceleration of the

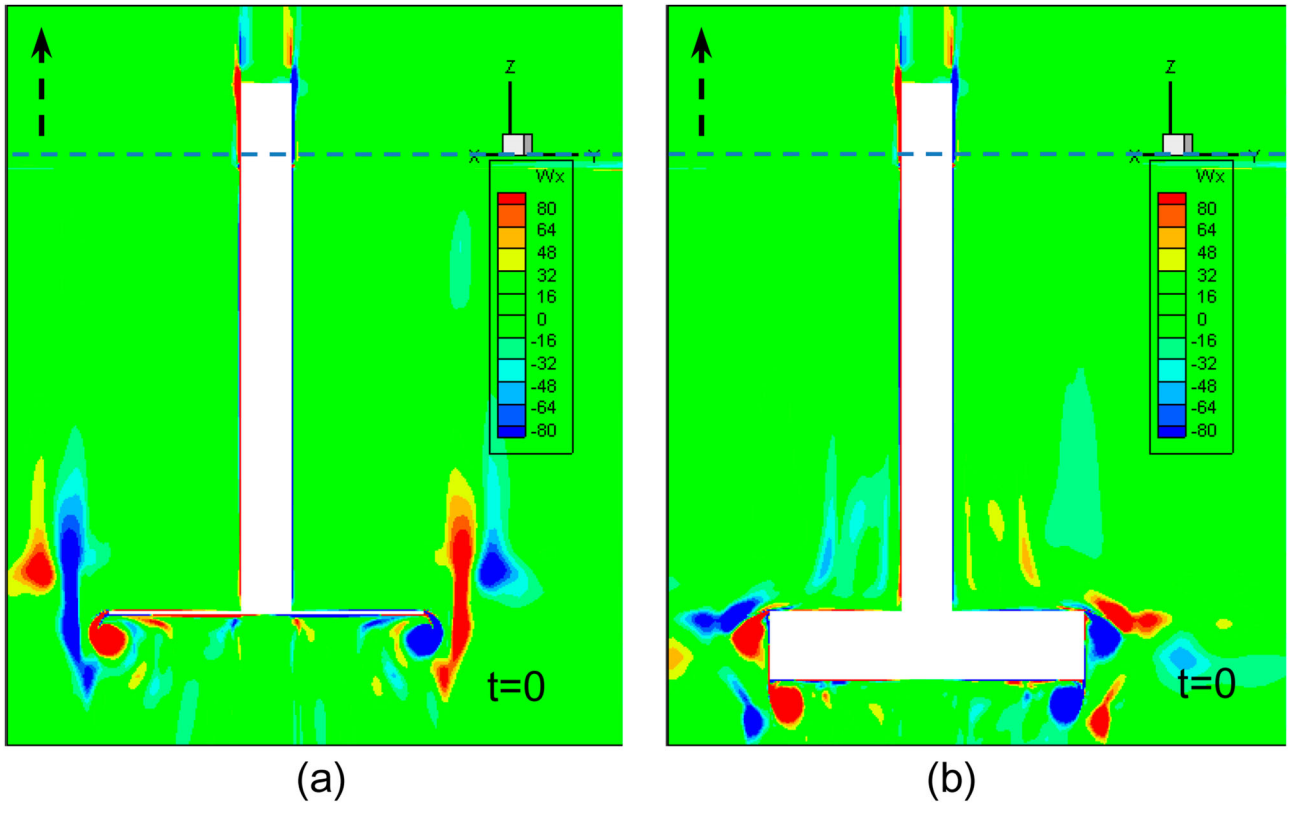

Figure 7. Instantaneous vortex patterns around the two heave plates with different aspect ratios at oscillating time t = 0. At this moment, the model is moving upward. The non-dimensional vorticity shown in the figure is defined as $W_X^* = W_X \times \omega$. ω is oscillating angular frequency (a) r_t = 0.01 and (b) r_t = 0.2. (This figure is available in colour online.)

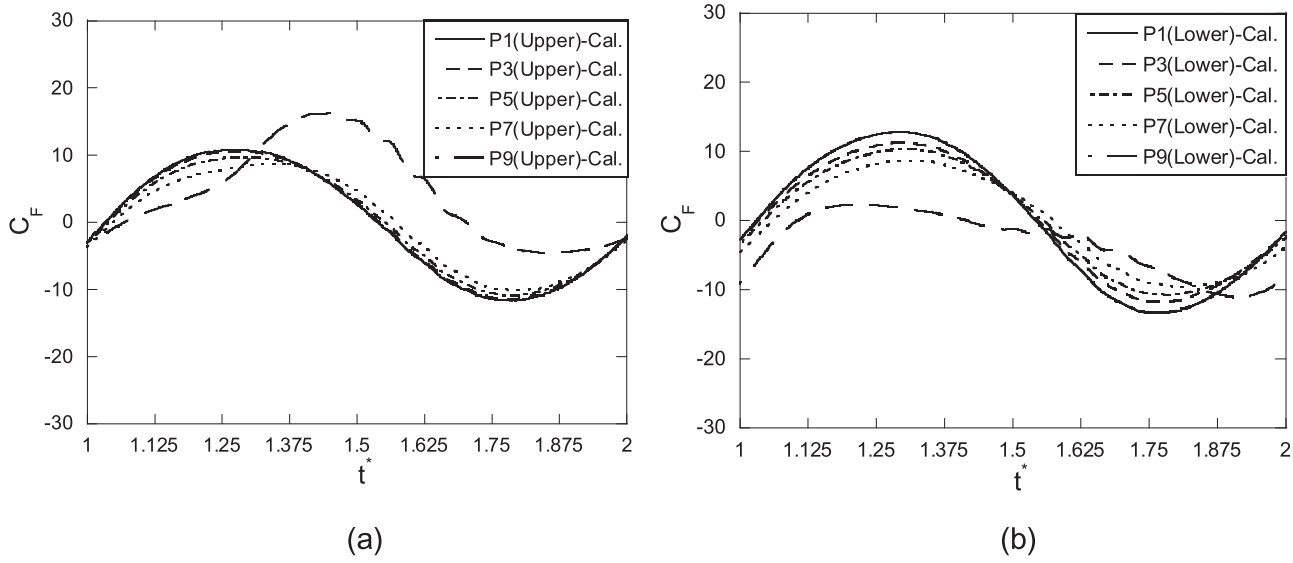

Figure 8. Time series of the non-dimensional hydrodynamic force acting on upper and lower surfaces for each panel of the plate. Value of non-dimensional hydrodynamic force on the adjacent panel is close, the forces on every two panels (P1, P3, P5, P7 and P9) are shown in these figures for a better view. Definition of each panel is shown in Figure 2 (a) Upper surface and (b) Lower surface.

moving model reaches its maximum. This indicates that the inertia force relating to added mass is dominant compared with the drag force. In contrast, the maximum force on the upper surface of panel P9 occurs at time $t = 4/8$ T when velocity of the moving model reaches its maximum, which indicates the drag force is dominant for the most outer panel. From Figure 8(b), the hydrodynamic forces on the lower surface are comparable with those on the upper surface except for the panel P9. Magnitude of hydrodynamic force on panel P9 is smaller than that on the other panels since the primary source of drag force most comes from the outer panel and it is the upper surface that provides the most drag force. Moreover, as for panel P1~P7, the hydrodynamic force on the upper surface is in phase with that on the lower surface owing to the characteristic distribution of dynamic pressure as shown in Figure 9. The maximum hydrodynamic force on the upper surface of panel P1 is slightly smaller than that on the lower surface because the column is attached on the upper surface, and thus, the area of upper surface of panel P1 is smaller.

Figure 9 shows dynamic pressure distribution on the *xz*-plane, upper surface, and lower surface of the plate in one oscillating period. A pair of positive and negative dynamic pressure is found on the upper and lower surface at time $T +$ 2/8 T or $T + 6/8$ T. At time $T + 2/8$ T, the dynamic pressure on the upper or lower surfaces gradually decreases from its centre to the outer panels, which directly leads to the gradual decrease in the hydrodynamic force as shown in Figure 8(a). The resulting force on the panel P8 decreases by 34% compared with that on the panel P1. At the moment $T + 4/8$ T, significant negative dynamic pressure is found on the outermost panel of the upper surface, which causes a large non-dimensional hydrodynamic force on the panel P9 as shown in Figure 8(a).

The resultant force acting on each panel, $F_{H,Pi}(t)$, is calculated as follows:

$$F_{H,Pi}(t) = F^U_{H,Pi}(t) + F^L_{H,Pi}(t) \tag{21}$$

where $F_{Pi}(t)$ is the resultant force on the panel Pi, $F^U_{H,Pi}(t)$ is a force on the upper surface of the panel Pi and $F^L_{H,Pi}(t)$ is the force on the lower surface of the panel Pi.

Added mass coefficient of each panel is obtained from Equation (15) as follows:

$$C_{a,Pi} = \frac{3M_{add,Pi}}{\rho_w(D^3_{Pi,outer} - D^3_{Pi,inner})},\ M_{add,Pi} = \frac{1}{\pi\omega a}\int_0^T F_{H,Pi}(t)\sin(\omega t)dt \tag{22}$$

where $M_{add,Pi}$ is the calculated added mass of the panel Pi and $D_{Pi,outer}$ and $D_{Pi,inner}$ are the outer and inner diameter of the panel Pi, respectively. Similarly, C_d for each panel Pi is defined with respect to the characteristic area of corresponding panel as

$$C_{d,Pi} = -\frac{3}{4\rho_w A\omega a^2}\int_0^T F_{H,Pi}(t)\cos(\omega t)dt \tag{23}$$

Figure 10 shows the distributed C_a and C_d of each panel with different aspect ratios. represents the distance of panel to the heave plate centre. $r = 0$ means the heave plate centre and $r = 1$ locates at the outer edge of the heave plate. Three sets of data with aspect ratio 0.01, 0.03 and 0.2 are shown in the figure. Similar to the integral C_a, the distributed C_a shown in Figure 10(a) exhibits weak dependence with aspect ratios. The C_a decreases dramatically from the centre to the outer edge because of the reduction of resultant force. As for the C_d shown in Figure 10 (b), it keeps stable in the inner part of the plate and increases significantly near the outer edge, which is consistent with the conclusion about the load distribution shown in Figures 8 and 9. The C_d for the outer panel exceeds 15 in the case of $r_t = 0.01$ and the C_d for the inner panel shows an increasing tendency as aspect ratio decreases. Therefore, decreasing the thickness of plate or adding the thin skirt at the outer edge of plate would be effective for increasing hydrodynamic damping of platform in its vertical direction.

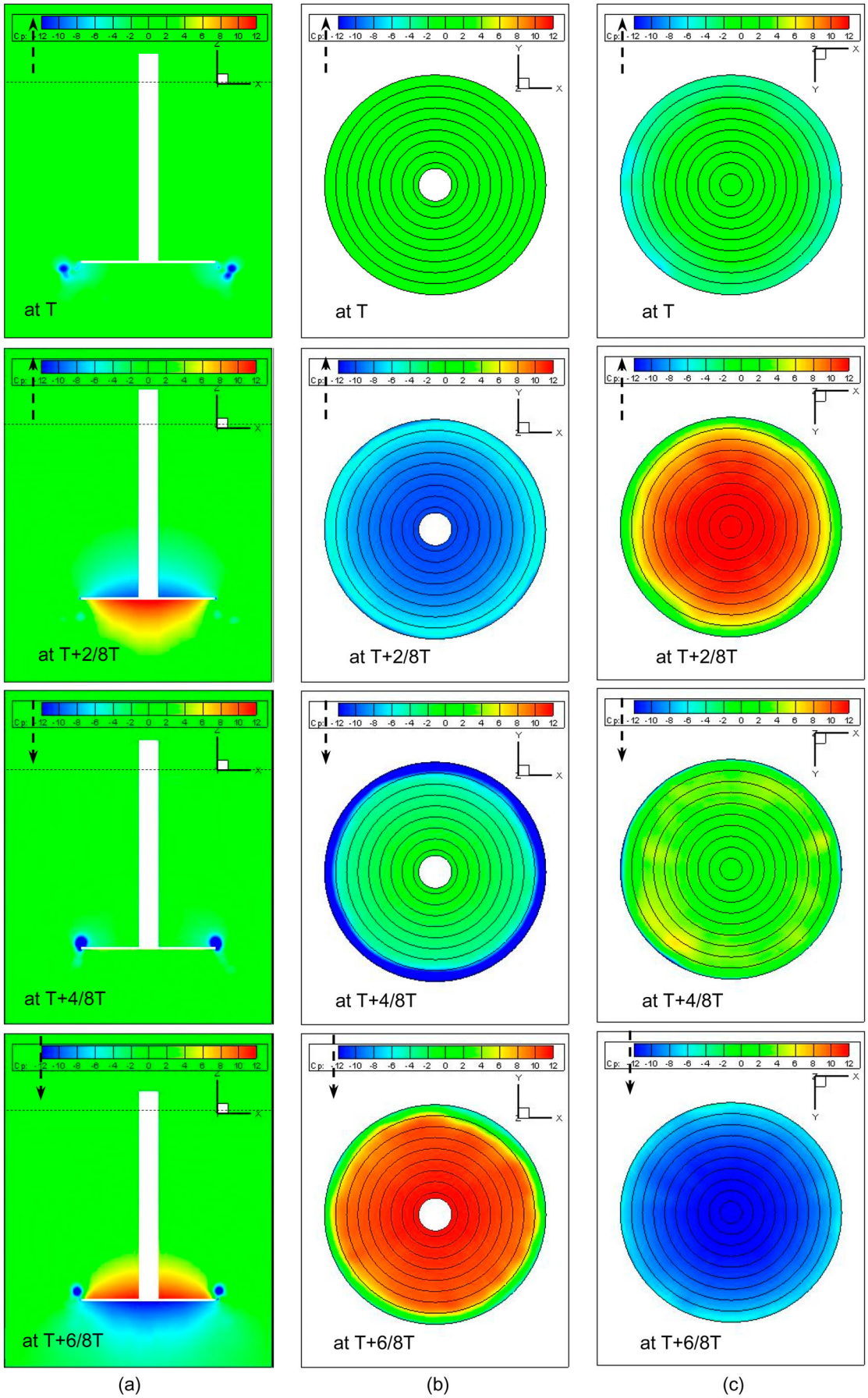

Figure 9. Four moments of distribution of dynamic pressure on the *x*–*z*, upper and lower surface of plate within one oscillating period. Fifth instant is same as first. At moment $t = T$, the model is starting to move upward. The model shown here has the diameter ratio $R_d = 6.68$ and aspect ratio $r_t = 0.02$ (a) xz plane, (b) Upper surface and (c) Lower surface. (This figure is available in colour online.)

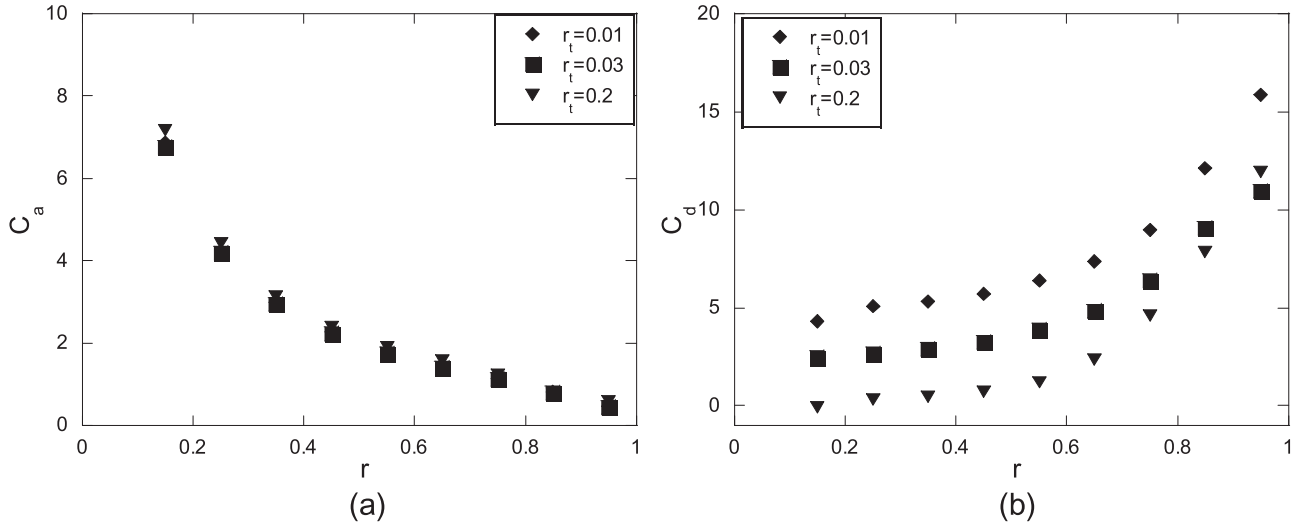

Figure 10. Variation of the distributed added mass and drag coefficients of the panel with the radius for different aspect ratios (a) Added mass coefficient and (b) Drag coefficient.

Figure 11 presents the distributed C_a and C_d of each panel varying with different diameter ratios. Two sets of data with diameter ratio 6.68 and 2.5 are shown in the figure. The diameter ratio is changed by varying the diameter of the attached column. In the case of large diameter ratio, inner part of the upper surface does not experience hydrodynamic force. As a result, C_a of the panel occupied by the column decreases significantly as shown in Figure 11(a). This is also true for the distributed C_d on the inner panels as shown in Figure 11(b), while C_a and C_d of the other panels remain unchanged.

By rewriting Equation (14), time series of total hydrodynamic force on panel Pi is reproduced in the form of Morison's equation as follows:

$$F_H,Pi(t) = \frac{1}{3}C_{a,Pi}\rho_w(D^3_{Pi,outer} - D^3_{Pi,inner})a\omega^2\sin(\omega t) - \frac{1}{2}C_{d,Pi}\rho_w A(a\omega)^2|\cos(\omega t)|(\cos(\omega t)) \quad (24)$$

where $C_{a,Pi}$ and $C_{d,Pi}$ are the added mass and drag coefficient obtained from Equations (22) and (23).

The time series of the non-dimensional hydrodynamic force is expressed as follows:

$$C_F(t^*) = \frac{F_H(t)}{\frac{1}{2}\rho_w A(\omega a)^2};\ t^* = \frac{t}{T} \quad (25)$$

As observed from Figure 8, the magnitude of hydrodynamic force on the upper surface for each panel of the plate is close to that on the lower surface. By assuming the hydrodynamic force on upper and lower surface of each panel is same, the non-dimensional hydrodynamic force can be expressed as follows:

$$C^{Upper}_{F,Pi}(t^*) = C^{Lower}_{F,Pi}(t^*) = \frac{1}{2}C_{F,Pi}(t^*) \quad (26)$$

Comparison of calculated and reproduced non-dimensional hydrodynamic force on upper and lower surface of the heave plate is shown in Figure 12. Except for panel 9, reproduced

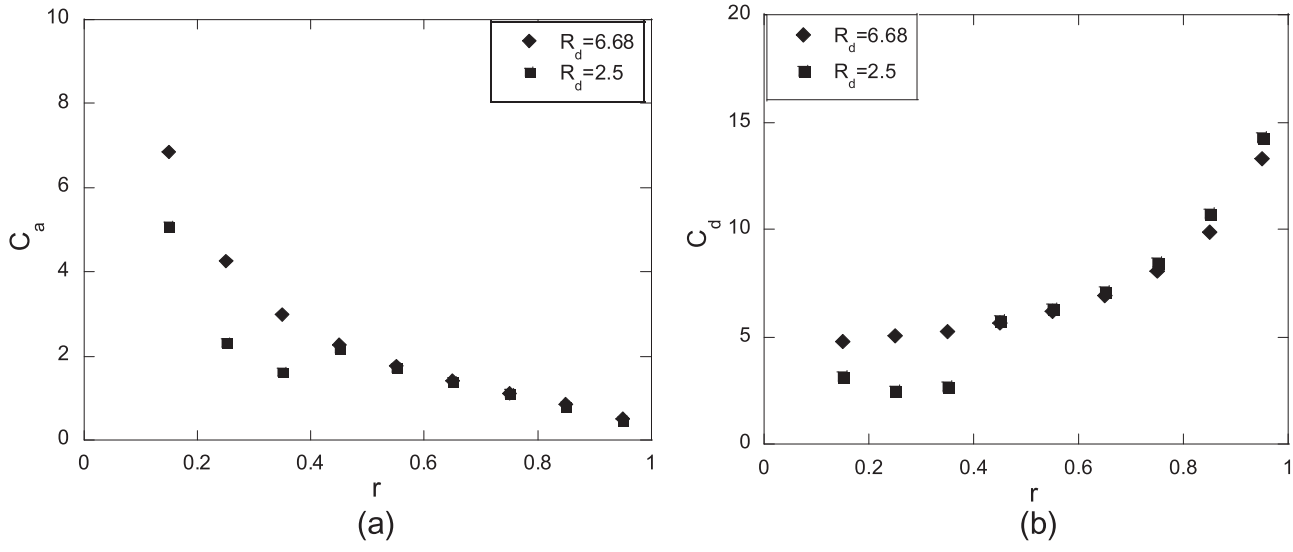

Figure 11. Variation of the distributed added mass and drag coefficients of the panel with the radius for different diameter ratios (a) Added mass coefficient and (b) Drag coefficient.

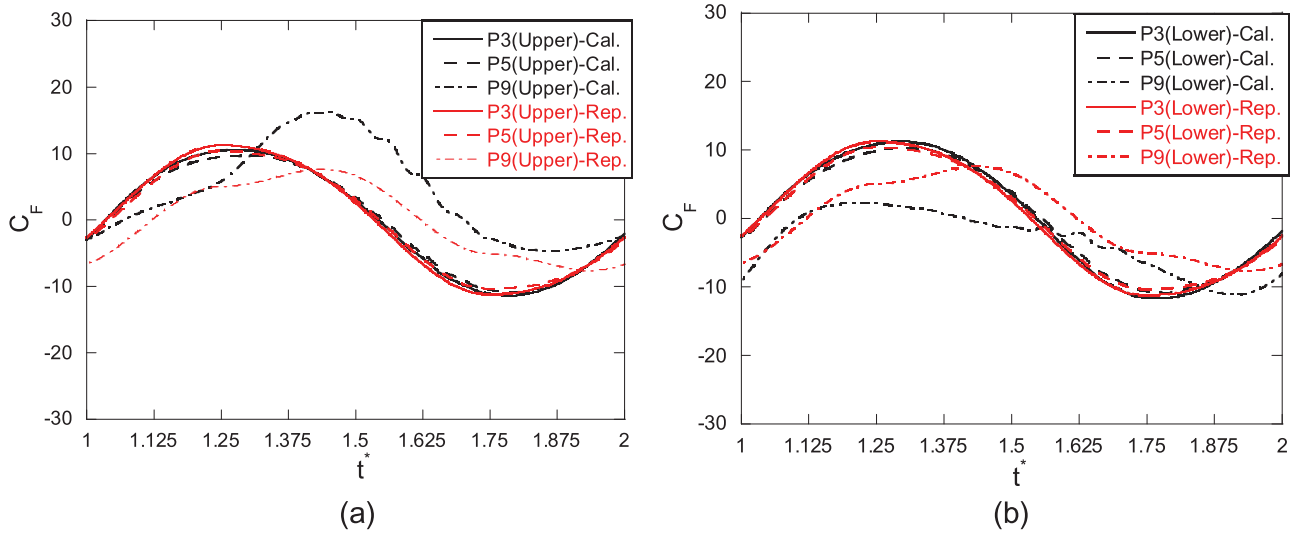

Figure 12. Time series of the reproduced non-dimensional hydrodynamic force acting on upper and lower surfaces for each panel of the plate. Value of non-dimensional hydrodynamic force on the adjacent panel is close, the forces on every two panels (P3, P5, P9) are shown in these figures for a better view. Definition of each panel is shown in Figure 2 (a) Upper surface and (b) Lower surface. (This figure is available in colour online.)

force shows a good agreement with the calculated force in terms of both magnitude and phase, proving that the distributed force on each panel could be predicted via a form of Morison's equation once the corresponding added mass and drag coefficient are determined. As for panel 9, magnitude of hydrodynamic force on upper surface is underestimated while the force on lower surface is overestimated, reflecting the deficiency of Morison's equation in the prediction of hydrodynamic force on the outer panel where drag force is dominant. In the next section, formulas of radially distributed C_a and C_d are proposed to predict the distributed hydrodynamic force via Equation (24) for structural design.

3.3. Formulas of radially distributed C_a and C_d

In this section, formulas of radially distributed C_a and C_d are proposed. The formulas of integral C_a and C_d are proposed and validated by Zhang and Ishihara (2018). The distributed C_a is assumed to follow an exponential function of Ae^{-Br}. The decay factor B is identified according to the distributed C_a as shown in Figure 10(a) and the coefficient A is evaluated by ensuring the integrated C_a equals to the total value given by the formula proposed by Zhang and Ishihara (2018). In order to consider the effect of column on the upper surface, a piecewise function is proposed and a reduction of 50% is applied since the hydrodynamic force within the region occupied by the column is zero, while that in the outer region is unchanged. Consequently, formula of the radially distributed C_a is expressed as follows:

$$C_a = \begin{cases} 7.23(1+0.2KC)^3 e^{-2.9r}; r > 1/R_d \\ 0.5(7.23(1+0.2KC)^3 e^{-2.9r}); r \le 1/R_d \end{cases} \quad (27)$$

where r is the normalised radial distance, KC refers to KC number and $R_d = D_{Hp}/D_c$ represents the diameter ratio.

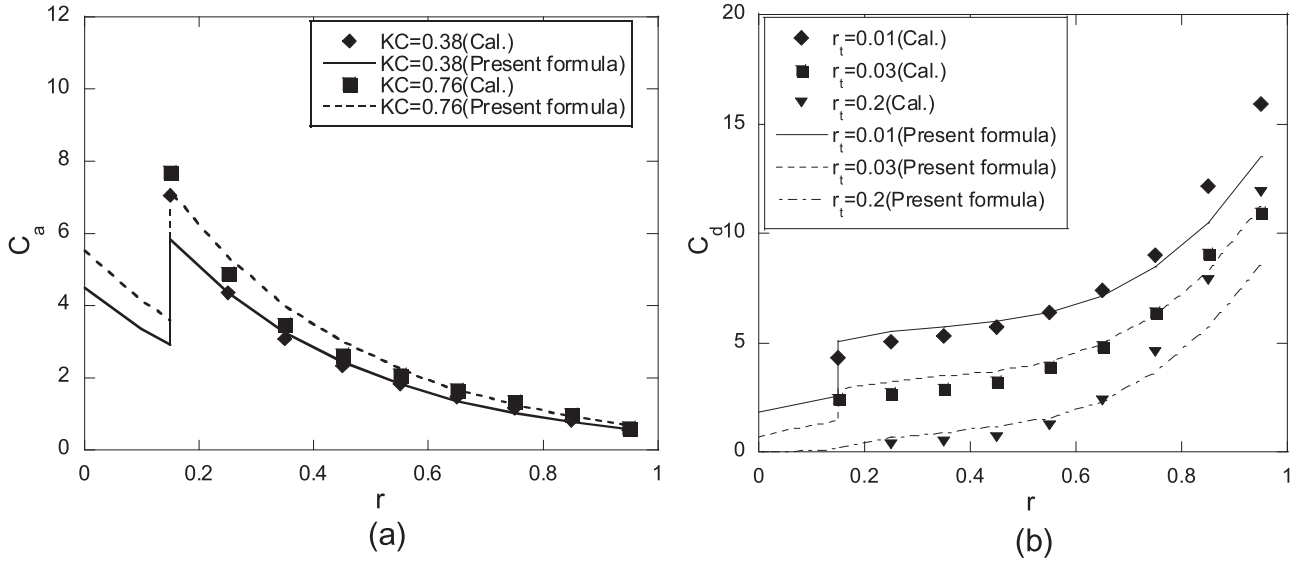

Figure 13. Comparison between the predicted hydrodynamic coefficients and the numerical results for different KC numbers and aspect ratios with $R_d = 6.68$ (a) Added mass coefficient and (b) Drag coefficient.

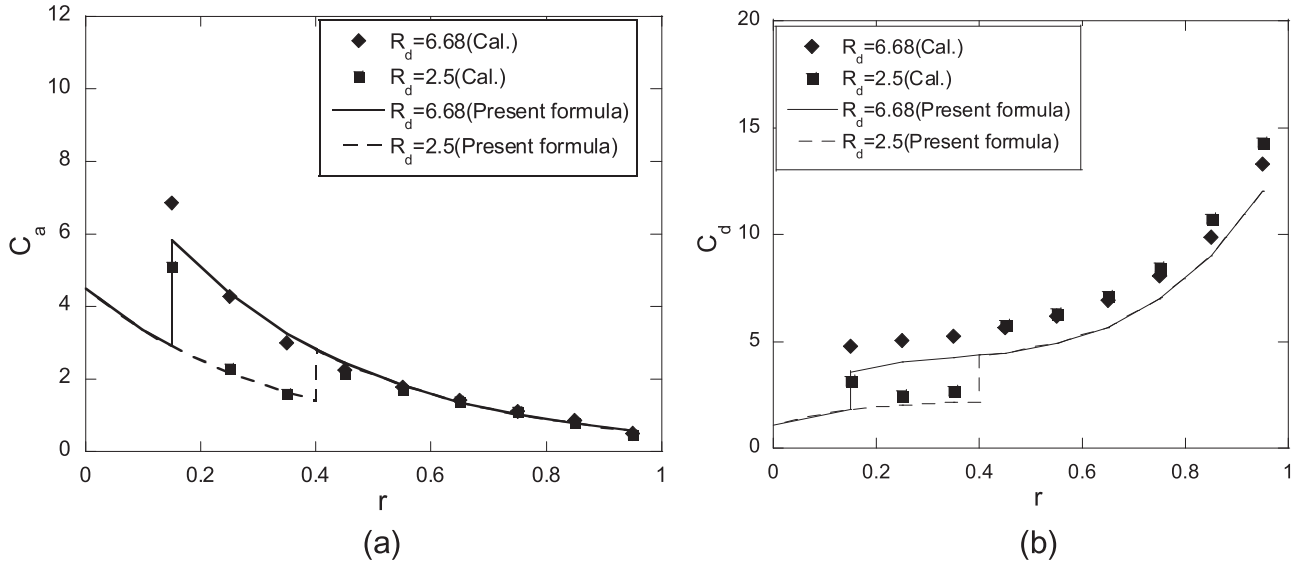

Figure 14. Comparison between the predicted predicted hydrodynamic coefficients and the numerical results for different diameter ratios with $r_t = 0.02$ and KC = 0.38 (a) Added mass coefficient and (b) Drag coefficient.

As with C_d, the three-order polynomial function is assumed and parameters are identified according to the distributed C_d as shown in Figure 10(b). By ensuring the integrated C_d equals to the value proposed by Zhang and Ishihara (2018), the formula of radially distributed C_d is expressed as follows:

$$C_d = \begin{cases} \max\{1.7r_t^{-1/3.7}(KC)^{-1/2.5} - 5.08 + 13.9r - 33.4r^2 + 31.3r^3, 0\}; r > 1/R_d \\ 0.5[\max\{1.7r_t^{-1/3.7}(KC)^{-1/2.5} - 5.08 + 13.9r - 33.4r^2 + 31.3r^3, 0\}]; r \le 1/R_d \end{cases} \quad (28)$$

where $r_t (= t_{Hp}/D_{Hp})$ is the aspect ratio, t_{Hp} is the thickness, and D_{Hp} is the diameter of heave plate.

Figure 13 shows comparison between the predicted hydrodynamic coefficients and the numerical results for different KC numbers and aspect ratios with $R_d = 6.68$. In Figure 13(a), KC = 0.38 represents the oscillating amplitude of $a = 0.02$ m, and $a = 0.04$ in the case of KC = 0.76. The diameter ratio $R_d = 6.68$ and aspect ratio $r_t = 0.02$ remain unchanged in the study of KC number effect. In Figure 13(b), KC = 0.38 and $R_d = 6.68$ remain unchanged in the study of aspect ratio effect. The distribution of C_a predicted by proposed formula matches well with the numerical results for the different KC numbers as shown in Figure 13(a). From Figure 13(b), the shape of C_d predicted by proposed formula shows good agreement with the numerical results for the different aspect ratios especially in the region near the plate centre, while the proposed formula underestimates the C_d near the edge of the plate. The change of vortex shedding pattern around the edge of plate makes the prediction of C_d far more complex which is expected to be improved in future study by introducing one specific parameter to consider the vortex shedding pattern change.

Figure 14 presents a comparison between the predicted hydrodynamic coefficients and the numerical results for different diameter ratios with $r_t = 0.02$. The proposed piecewise function of C_a matches well with the numerical results. The distributed C_d by the proposed formula is slightly underestimated due to the underestimation of total C_d for this aspect ratio of 0.02.

4. Conclusions

In this study, distributed hydrodynamic coefficients of circular heave plates in the radial direction are investigated by numerical simulations for different diameter and aspect ratios. The conclusions are summarised as follows:

1. The distributed hydrodynamic force on the heave plate is investigated by the flow visualisation. The hydrodynamic load decreases with the distance from the centre of heave plate and the difference in the time series of the hydrodynamic forces on the inner and the outermost panels is caused by the vortex shedding around the outer edge of heave plate.
2. The added mass coefficient decreases with the distance from the plate centre to the outer edge, while the drag coefficient increases from the centre to the outer edge due to the vortex shedding at the outer edge of the plate. In addition, the effect of aspect and diameters on the distributed hydrodynamic coefficients shows the same tendency as the whole hydrodynamic coefficient of the heave plate.
3. Formulas of the distributed C_a and C_d in the radial direction are proposed and validated by the present numerical simulations. The predicted distributions of C_a and C_d show

favourable agreement with the numerical simulations for different diameter and aspect ratios.

Acknowledgements

This research is carried out as a part of the Fukushima floating offshore wind farm demonstration project funded by the Ministry of Economy, Trade and Industry. The authors wish to express their deepest gratitude to the concerned parties for their assistance during this study.

Disclosure statement

No potential conflict of interest was reported by the authors.

References

Amabili M, Frosali G, Kwak MK. 1996. Free vibrations of annular plates coupled with fluids. J Sound Vibr. 191:825–846.

Ansys. 2012. Fluent theory guide. Canonsburg, PA: Ansys Inc.

Askari E, Jeong KH, Amabili M. 2013. Hydroelastic vibration of circular plates immersed in a liquid-filled container with free surface. J Sound Vib. 332:3064–3085.

Browning J, Jonkman J, Robertson A, Goupee A. 2014. Calibration and validation of a spar-type floating offshore wind turbine model using the FAST dynamic simulation tool. Proceedings of the Journal of Physics: Conference Series; 2014; Oldenburg, Germany: IOP Publishing.

Chandrasekaran S, Madhavi N. 2014. Variation of water particle kinematics with perforated cylinder under regular waves. Busan, South Korea: ISOPE.

Chandrasekaran S, Madhavi N. 2015a. Retrofitting of offshore cylindrical structures with different geometrical configuration of perforated outer cover. Int J Shipbuild Prog. 62(1-2):43–56.

Chandrasekaran S, Madhavi N. 2015b. Design aids for offshore structures with perforated members. Ships Offshore Struct. 10:21.

Chandrasekaran S, Madhavi N. 2015c. Flow field around outer perforated circular cylinder under regular waves: numerical study. Mar Syst Ocean Technol. 10:1–10.

Chandrasekaran S, Madhavi N. 2016. Variation of flow field around twin cylinders with and without the outer perforated cylinder – numerical study. China Ocean Eng. 30:763–771.

Chandrasekaran S, Madhavi N, Sampath S. 2015. Estimation of force reduction on ocean structures with perforated members. Proceedings of 34th International Conference on Ocean, Offshore and Arctic Engineering (OMAE2015); May 31 - June 5, 2015; St. John's, NL, Canada.

Fukushima. 2013. FORWARD. http://www.fukushima-forward.jp/english/index.html.

Garrido-Mendoza CA, Thiagarajan KP, Souto-Iglesias A, Colagrossi A, Bouscasse B. 2015. Computation of flow features and hydrodynamic coefficients around heave plates oscillating near a seabed. J Fluids Struct. 59:406–431.

Graham J. 1980. The forces on sharp-edged cylinders in oscillatory flow at low Keulegan–Carpenter numbers. J Fluid Mech. 97:331–346.

Holmes S, Bhat S, Beynet P, Sablok A, Prislin I. 2001. Heave plate design with computational fluid dynamics. J Offshore Mech Arct Eng. 123:22–28.

Hywind. 2009. We energize the lives of 170 million people. Every day. https://www.equinor.com/.

Ishihara T, Zhang S. 2019. Prediction of dynamic response of semi-submersible floating offshore wind turbine using augmented Morison's equation with frequency dependent hydrodynamic coefficients. Renewable Energy. 131:1186–1207.

Jonkman JM. 2007. Dynamics modeling and loads analysis of an offshore floating wind turbine. ProQuest, technical Report NREL/TP-500-41958.

Kvittem MI, Bachynski EE, Moan T. 2012. Effects of hydrodynamic modelling in fully coupled simulations of a semi-submersible wind turbine. Energy Procedia. 24:351–362.

Li J, Liu S, Zhao M, Teng B. 2013. Experimental investigation of the hydrodynamic characteristics of heave plates using forced oscillation. Ocean Eng. 66:82–91.

Lopez-Pavon C, Souto-Iglesias A. 2015. Hydrodynamic coefficients and pressure loads on heave plates for semi-submersible floating offshore wind turbines: A comparative analysis using large scale models. Renewable Energy. 81:864–881.

Oka S, Ishihara T. 2009. Numerical study of aerodynamic characteristics of a square prism in a uniform flow. J Wind Eng Ind Aerodyn. 97:548–559.

Philip NT, Nallayarasu S, Bhattacharyya S. 2013. Experimental investigation and CFD simulation of heave damping effects due to circular plates attached to spar hull. Ships Offshore Struct. 14(4):396–411.

Phuc PV, Ishihara T. 2007. A study on the dynamic response of a semi-submersible floating offshore wind turbine system Part 2: numerical simulation. ICWE12 Cairns, Australia. p. 959–966.

Sarpkaya T. 2010. Wave forces on offshore structures. Cambridge University Press.

Smagorinsky J. 1963. General circulation experiments with the primitive equations. I. The basic experiment. Month Wea Rev. 91:99–164.

Stern F, Wilson RV, Coleman HW, Paterson EG. 2001. Comprehensive approach to verification and validation of cfd simulations—part 1: methodology and procedures. J Fluids Eng. 123(4):792.

Tao L, Cai S. 2004. Heave motion suppression of a spar with a heave plate. Ocean Eng. 31:669–692.

Tao L, Dray D. 2008. Hydrodynamic performance of solid and porous heave plates. Ocean Eng. 35:1006–1014.

Tao L, Lim KY, Thiagarajan K. 2004. Heave response of classic spar with variable geometry. J Offshore Mech Arct Eng. 126:90–95.

Tao L, Molin B, Scolan Y-M, Thiagarajan K. 2007. Spacing effects on hydrodynamics of heave plates on offshore structures. J Fluids Struct. 23:1119–1136.

Tao L, Thiagarajan K. 2003a. Low KC flow regimes of oscillating sharp edges I. Vortex shedding observation. Appl Ocean Res. 25:21–35.

Tao L, Thiagarajan K. 2003b. Low KC flow regimes of oscillating sharp edges. II. Hydrodynamic forces. Appl Ocean Res. 25:53–62.

Utsunomiya T, Shiraishi T, Sato I, Inui E, Ishida S. 2014. Floating offshore wind turbine demonstration project at Goto Islands, Japan. Proc Oceans. 1–17.

Waris MB, Ishihara T. 2012. Dynamic response analysis of floating offshore wind turbine with different types of heave plates and mooring systems by using a fully nonlinear model. Coupled Syst Mech. 1:247–268.

WindFloat. 2011. Oregon's clean energy future. Available from http://windfloatpacific.com/.

Yang J, Tian X, Li X. 2014. Hydrodynamic characteristics of an oscillating circular disk under steady in-plane current conditions. Ocean Eng. 75:53–63.

Zhang S, Ishihara T. 2018. Numerical study of hydrodynamic coefficients of multiple heave plates by large eddy simulations with volume of fluid method. Ocean Eng. 163:583–598.